Electrochemical studies and phase-structural characterization of a high-capacity La-doped AB_2 Laves type alloy and its hydride

ChuBin Wan[1,2], R.V. Denys[2,3],

M. Lelis[4], D. Milčius[4], V.A.Yartys[2,5*)]

[1] University of Science and Technology Beijing, 100083, China

[2] Institute for Energy Technology, P.O. Box 40, Kjeller NO-2027, Norway

[3] HYSTORSYS AS, P.O. Box 45, Kjeller NO-2027, Norway

[4] Center for Hydrogen Energy Technologies,

Lithuanian Energy Institute, Kaunas, Lithuania

[5] Norwegian University of Science and Technology, Trondheim, Norway

ABSTRACT

This work was focused on studies of structural and electrochemical properties of the La-doped AB_2-type Zr/Ti-based metal hydride anode alloys. The $Ti_{0.2}Zr_{0.8}La_{0-0.05}Ni_{1.2}Mn_{0.7}V_{0.12}Fe_{0.12}$ alloys were characterized using SEM, EDS and XRD, which concluded that the major C15 Laves type AB_2 compound co-exists with a minor La-Ni intermetallic. NPD study indicated that vanadium together with Ti and Zr partially fills the A site, while the rest of V together with Ni, Mn and Fe statistically fills the B site. NPD showed that in a trihydride $(Ti,Zr,V)(Ni,Mn,Fe,V)_2D_{2.9}$ D atoms occupy A_2B_2 tetrahedra. The alloys

were characterized during high-rate discharge and on cycling. La addition resulted in a significant improvement of the activation performance caused by a catalytic influence of LaNi hydride. The highest content of La greatly accelerated the activation, but it also caused an obvious decrease in discharge capacity and cycling stability. The alloy with an optimized La addition (x= 0.03) demonstrated a maximum discharge capacity of 420 mAh g^{-1} and the discharge capacity maintained at 79 % at 0.71 C, while the capacity retention after 500 cycles was also high, 63 %. Based on the EIS results, we conclude that the decay of the alloy electrode is related to the irreversible capacity loss and its pulverization.

Keywords

Metal hydrides; Laves type intermetallic; Electrochemical performance; Neutron powder diffraction; Metal hydride battery anode.

---

*) Corresponding author: volodymyr.yartys@ife.no. Tel. +47 454 22 065.

1. Introduction

A nickel-metal hydride (Ni/MH) battery is an important for the consumers battery technology, which finds a broad variety of applications in portable, stationary, and mobile energy storage [1, 2]. AB_2, AB_3 and A_2B_7 MH alloys are used as active negative electrode materials, with discharge capacities exceeding 400 mAh g^{-1} [1]. The AB_2 alloys show higher storage capacities and benefit from lower raw material costs as compared to the AB_3 and A_2B_7 alloys, which contain up to 30 wt.% of expensive and limited in resources rare earth (RE) metals [3, 4]. However, the AB_2 alloys suffer from a slow activation, insufficient rate capabilities and limited cycle durability [2, 5]. The current work is focused on addressing these three technological challenges, aiming at meeting the demands for the advanced Ni/MH battery applications.

Numerous AB_2 alloys can absorb hydrogen to form hydrides, and Ti/Zr-based AB_2-type alloys have been developed as second-generation alloys for Ni/MH battery applications owing to their high values of energy densities related to the formation of the AB_2H_{3-4} hydrides [6]. Multi-element Ti/Zr-based AB_2-type alloys typically contain Ti and Zr as A-components, and Ni, V, Cr, Mn, Co, Al, Fe as B-components; the discharge capacities of these alloys cover a range from 370 mAh g^{-1} to 450 mAh g^{-1} [2].

In Zr-based AB_2-type alloys, a substitution of Zr for Ti is possible and it has a strong effect on the structure and electrochemical performances of these alloys which vary depending on the alloy systems [7, 8]. The discharge capacities of the electrodes are strongly related to the phase composition of the alloys. Sun et al. [9] reported that the abundance of the C14 Laves

phase increases and the abundances of the C15 Laves phase and non-Laves phases decrease as the amount of Ti additive increases.

In earlier published reference works [3, 9-11], a range of rare earth metals including La, Ce and Nd has been tried as additives to the Zr and Zr/Ti based Laves type alloys used as metal hydride battery anodes. These studies revealed that independent of the composition of the base alloy, additives in the amounts reaching 0.05 and even 0.1 at. RE / f.u. AB_2 improved the activation performance but at the same time caused negative changes decreasing the discharge capacity and cycle durability. However, the cycling performance has not been sufficiently characterized being limited to just 30 cycles. Thus, a more systematic and detailed study is in urgent need to address two topics: (a) Which RE content gives the best overall electrochemical performance of the battery anodes; (b) How to optimize a long cycle performance and performance at high discharge current densities as related to the amount of the rare earth additive. These topics were addressed in the present study.

In multi-element AB_2-type alloys [2], constituting elements contribute to the H storage performance in a variable way. Indeed, Ti, Zr and V are the hydride forming elements, Ni has a high catalytic activity in redox reactions, Co and Mn provide surface activity relevant for hydrogen reduction and oxidation, and Cr, Al and Fe increase the corrosion resistance. In the present paper, we are focusing on studies of one type of these alloys, $Zr_{0.8}Ti_{0.2}La_{0.01-0.05}Ni_{1.2}Mn_{0.7}V_{0.12}Fe_{0.12}$, containing additions of La and Fe elements for improving activation performance and cycling stability. These alloys were suggested as prospective electrode materials in our earlier studies [12]. In the current work we present

results of a detailed characterization of the annealed Zr/Ti-based AB_2 alloy aimed at establishing a relationship between the composition, phase structure and electrochemical properties and at optimizing the criteria for selecting the materials with advanced electrode performance.

2. Experimental

2.1. Alloy synthesis and annealing

$Ti_{0.2}Zr_{0.8}La_{0.01-0.05}Ni_{1.2}Mn_{0.7}V_{0.12}Fe_{0.12}$ alloys were prepared through arc melting by using stoichiometric ratios of the constituting elements (purity was higher than 99.7% in each case). As Mn is subjected to a partial vaporization at high melting temperatures, the amount of Mn added to the composition of the mixture for the melting was increased by 4% in order to compensate for the losses during the sample preparation. The arc melting was performed on a water-cooled copper hearth when using high purity Ar gas (99.999%; pressure 0.1 MPa). Approximately 10-gram alloys were prepared and were remelted 4 times to ensure their homogeneity. The as-cast alloy ingots were sealed in stainless steel sample tubes filled with Ar and then transferred into an annealing furnace. These alloys were annealed at 950 °C for 10 h and then quenched into cold water (4 °C) resulting in a homogenization of the alloy.

2.2. Structural characterization

A Bruker D8 Advance X-ray diffractometer was used to study the phase structural composition of the alloys using V-Ray diffraction (XRD). The XRD data were collected in a 2θ

range 20–80° using a step size of 0.01° and using a Cu Kα radiation source (λ=1.5406 Å). Powder diffraction data were analyzed by Rietveld whole-profile refinements by using the General Structure Analysis System software [13]. The microstructure of the samples was analyzed by a Hitachi S-3400N scanning electron microscope (SEM) equipped with energy dispersive spectroscopy (EDS) detector Bruker XFlash QUAD 5040.

Neutron powder diffraction (NPD) studies were performed at a SINQ Neutron Source, Paul Scherrer Institute, Switzerland, by using an HRPT Diffractometer [14] working in a high-intensity mode (λ=1.494 Å; 2θ range 3.8°–164.75° with a step size of 0.05°). The deuteride prepared from the $Ti_{0.2}Zr_{0.8}La_{0.03}Ni_{1.2}Mn_{0.7}V_{0.12}Fe_{0.12}$ alloy was synthesized using gaseous deuterium in a stainless steel container (wall thickness 0.2 mm; d_{inner} = 6 mm), which was connected to a Sievert's-type apparatus and used as a sample cell during the in situ NPD experiments [15]. The obtained neutron diffraction data were refined with the Rietveld method using the GSAS software [13].

2.3. Electrochemical characterization

MH anode electrodes were prepared for the electrochemical tests using the electrode preparation procedures which were detailed in our earlier publication [16]. MH alloy powder having a particle size of 40-60 μm was chosen to perform the electrochemical tests. Electrochemical properties were characterized at room temperature in a three-electrode system by using a 9 N KOH aqueous electrolyte. The system consisted of a MH working electrode, a sintered NiOOH/$Ni(OH)_2$ counter electrode, and a Hg/HgO reference electrode. Each anode electrode was fully activated at a 0.24 C rate during 10 charge-discharge (C/D) cycles. The high-rate dischargeability and cycling stability were subsequently evaluated, and

the cut-off potential of electrode discharge was set at −0.74 V versus Hg/HgO electrode.

Electrochemical impedance spectroscopy (EIS) measurements were performed using a VSP BioLogic Electrochemical Workstation at an amplitude of 10 mV in a frequency range of 1 mHz to 100 kHz. Prior to the measurements, the electrodes were subjected to 10, 100, 350, and 500 cycles and discharged to 50 % depth-of-discharge (DOD).

3. Results and discussion

3.1. Structural XRD analysis

Figure 1 shows the XRD patterns of the annealed $Zr_{0.8}Ti_{0.2}La_{0.03}Ni_{1.2}Mn_{0.7}V_{0.12}Fe_{0.12}$ alloy and the alloy electrodes after 30 and 500 cycles. Table 1 summarizes the refined crystallographic data, including unit cell lattice parameters and cell volumes.

Refinements showed that the annealed alloy contains only a C15 Laves phase with FCC structure. XRD powder profile refinements showed that the experimental and calculated pattern well agree with each other (Fig. 1).

MH battery anode electrodes were prepared using a powder mixture consisting of annealed alloy and carbonyl nickel (weight ratio 1:4). Even after 500 charge/discharge cycling, besides the Ni phase, only C15 phase was identified in the electrodes showing its high stability. No metal oxides appear in the cycled electrodes, and hence, it is reasonable to suggest that the oxidation is not primarily responsible for the cycle degradation of this La-containing AB_2 alloy.

The Zr-Ni and Ti-Ni phases were considered earlier to play an important role in improving the battery performance, including improvements of activation, high-rate capability, and cycle life [17-19]. However, neither Zr-Ni nor Ti-Ni phases were observed in the studied samples. Instead, a La-Ni intermetallic has been formed as a secondary phase. However, because of a small content of La (a few at.% in total), it was not possible to document the presence of La-based phase by XRD.

After the cycling, the crystallographic characteristics of the alloy (lattice parameters and cell volumes) were determined from XRD data and are given in Table 1. Compared with the virgin C15 phase before the electrochemical tests, the lattice constants and volumes of the unit cells of the C15 type intermetallic noticeably decreased after electrochemical activation, and they decreased further after 500 charge/discharge cycles, even though this extra decrease was relatively modest. The most plausible explanation for the observed changes is in the fact that metal elements are selectively dissolved from the negative electrode into the KOH electrolyte. Young et al. [20] found that V-containing AB_2 alloys leach out large amounts of V into the concentrated (30 wt.% KOH) electrolyte solution when exposed to this solution for 4 h. The leaching of Mo into the electrolyte was also reported for the Mo-addition AB_2 metal hydride alloys [21]. Severe leaching out of Mn and Al from the negative electrode after the cycling was reported for the Mn-modified A_2B_7 superlattice alloy system [22]. Furthermore, the leaching out of Mn and Al was also reported for the anodes of the AB_5-based Ni/MH batteries in [23]. In should be mentioned that the V-containing AB_2 alloy studied in [20] not only leached large amount of V, but also showed a more extensive dissolution of Zr, Ti, Al and Cr than the V-free alloys.

Thus, leaching of the components of the cycled negative electrodes into the alkaline solution appears to a general feature and can be directly linked to the behavior of the electrode material studied in the present study.

When trying to understand the behavior of the studied in the present work $Zr_{0.8}Ti_{0.2}La_{0.03}Ni_{1.2}Mn_{0.7}V_{0.12}Fe_{0.12}$ alloy we note some important related features. These are:

(a) Nickel appears to be a corrosion resistant component of the characterized for leaching in KOH solution metal hydride anode alloys;

(b) Nickel is a majority B-component of the studied in a current work $Zr_{0.8}Ti_{0.2}La_{0.03}Ni_{1.2}Mn_{0.7}V_{0.12}Fe_{0.12}$ alloy;

(c) Nickel has the smallest atomic size (r=1.246 Å) as compared to the other B-components (Mn: 1.264 Å; V: 1.346 Å; Fe: 1.274 Å).

When accounting these mentioned features together, one can conclude that enrichment in smaller in size nickel is likely to occur when the vanadium-containing studied alloy is submerged into a concentrated alkaline solution and this may cause contraction of the metal lattice. This is indeed the case. Furthermore, a process of selective dissolution would be facilitated by altering expansion and contraction of the alloy during its charge and discharge because of the formation and decomposition of the hydride phase ($\Delta a/a$=7.00 %; $\Delta V/V$= 22.5 %, see crystal structure data presented later in this paper). Thus, the fact that the alloy's lattice progressively shrinks (even though not so intensively when the number of the cycles is increased from 100 to 500 as compared to the difference between the virgin material and the material after 100 cycles) finds its reasonable explanation by assuming a selective leaching of the larger than Ni transition metals, first of all vanadium.

Furthermore, the metal atoms may undergo a redistribution with the formation of lattice defects, such as vacancies and dislocations during the charging-discharging (C/D) cycles. Hence the cell volume of AB_5 alloy frequently shows a decrease during the cycling as observed in [24, 25]. In contrast, some studies reported the opposite trends in the variation of lattice parameters [26, 27]. The lattice parameters of H storage alloys slightly increase after several absorption-desorption cycles, and this is ascribed to the formation of electrochemically stable against the discharge solid solution of hydrogen in the alloys. However, based on the above considerations, our results suggest that the amount of unreleased hydrogen remaining in the studied AB_2-type alloy was rather small.

Finally, one more feature should be discussed. It should be noted that Nakamura et al. [28] proposed that the presence of lattice defects may accompany long term cycling causing a loss of the reversible hydrogen storage capacity because of irreversible trapping of hydrogen atoms at the lattice defects. We assume that such a mechanism may indeed contribute to the performance observed in the present study during the cycling of the electrodes.

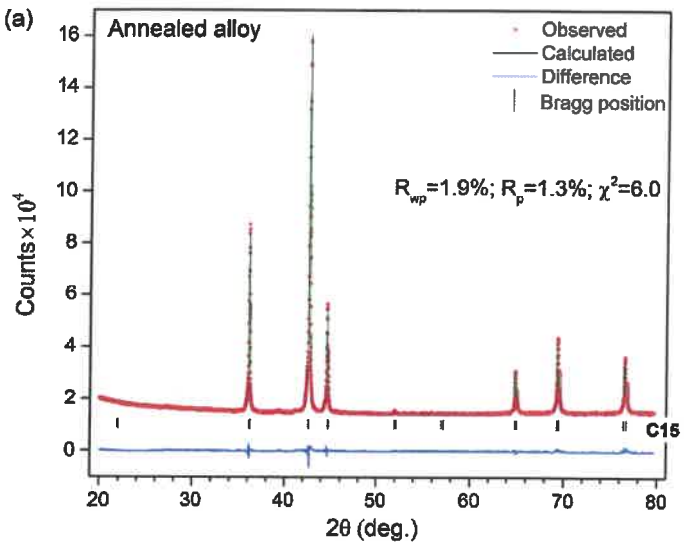
(a)
Annealed alloy
Observed
Calculated
Difference
Bragg position
R_{wp}=1.9%; R_p=1.3%; χ^2=6.0
Counts×10⁴
C15
2θ (deg.)

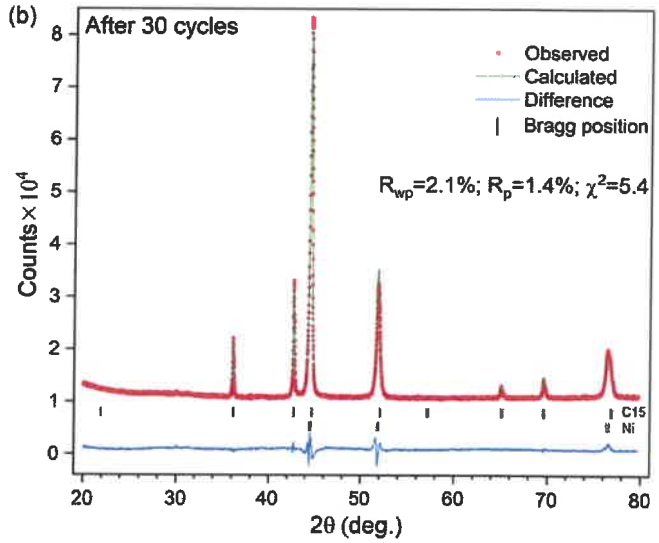
(b)
After 30 cycles
Observed
Calculated
Difference
Bragg position
R_{wp}=2.1%; R_p=1.4%; χ^2=5.4
Counts×10⁴
C15
Ni
2θ (deg.)

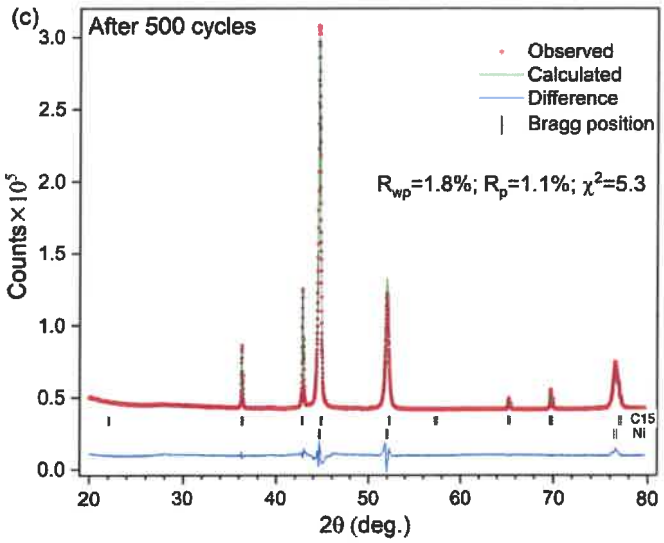

Fig. 1. Rietveld refinements of XRD profiles for the annealed alloy (a), after performing cycling of charge-discharge - 30 cycles (b) and 500 cycles (c) - of the alloy anode. Vertical ticks show the positions of the Bragg peaks of the phase constituents (C15 Laves type intermetallic and Ni foam).

Table 1.

Crystallographic data obtained during Rietveld refinements of the annealed alloy, and the electrodes containing this alloy after performing 30 and 500 cycles.

Samples	Phase	Space group	Unit cell parameters	
			a, Å	V, Å^3
Annealed	C15	$Fd\bar{3}m$	7.0441(1)	349.52(1)
30 cycles	C15	$Fd\bar{3}m$	7.0159(1)	345.34(1)
500 cycles	C15	$Fd\bar{3}m$	7.0096(0)	344.41(1)

Metal Ni phase present in a sample as a Ni foam is identified in the cycled electrodes but is not listed in Table 1 for simplicity. Abundance of the refined intermetallic was 100 % in each case.

3.2. Neutron diffraction studies of intermetallic alloy and its deuteride

The initial alloy sample was activated in vacuum at 573 K and charged by deuterium gas (99.8% purity) at room temperature and pressure of 5 bar for 24 h. Rapid deuteration took place and was finished in less than 1 hour; no further cycling was performed and the sample was used as synthesized during the initial charging in the NPD study. From pressure changes in the calibrated system, the D content in the synthesized deuteride was estimated as $AB_2D_{2.9}$ at. D/f.u. AB_2.

Figure 2 shows the experimentally measured (at 300 K) and calculated neutron diffraction patterns for the AB_2-type annealed alloy and its deuteride. In the annealed alloy, the experimental diffraction patterns can be attributed to the cubic C15-type structure (space group $Fd\bar{3}m$) with Ti, Zr, and V atoms in the 8*a* site and Ni, Mn, Fe, and V atoms in the 16*d* site. The V atoms occupy both of the 8*a* and 16*d* sites also in the deuteride of the annealed alloy (see Table 2). It is well known that Ti and V form a binary solid solution with unlimited solubility of the components, which in turn on hydrogenation forms a range of homogeneous $(Ti,V)H_2$ dihydrides at all possible ratios of Ti/V content [29, 30]. Thus, affinity of titanium to vanadium is high and when titanium becomes an A component in the $Zr_{0.8}Ti_{0.2}La_{0.03}Ni_{1.2}Mn_{0.7}V_{0.12}Fe_{0.12}$ alloy, this makes it possible for vanadium to partially reside at the A site together with Zr and Ti – which is indeed happening in the alloy and its hydride.

In the Rietveld powder refinements of the measured pattern for $AB_2D_{2.9}$ deuteride, the occupancies of the metal atoms were fixed to the values observed in the initial alloy. From the refinements, the positions and occupancy of deuterium atoms were obtained. It is known that deuterium atoms in the C15-type hydride $AB_2H_x(D)_x$ can occupy three types of interstitial sites: 96*g* (A_2B_2), 32*e* (AB_3) and 8*b* (B_4). In the initial refinements the most probable for H/D accommodation 96*g* and 32*e* sites were considered, but the refinements showed zero occupancy of the 32*e* and 8*b* sites. In further refinements, only the occupancies of 96*g* sites were refined yielding a total D content of 2.9 atoms D per formula unit. This value within experimental error limit agrees with the value determined from deuterium absorption experiments, $AB_2D_{2.9}$. Table 2 and Figure 2 present the crystal structure data and the reliability factors resulting from the refinements.

In the crystal structure of $AB_2D_{2.9}$ deuteride (see Figure 3), D atoms only partially occupy the A_2B_2 tetrahedra. The sole occupancy of the 96*g* sites (x, x, z) by D atoms at 300 K is consistent with the general trend observed for the Laves type Zr-based hydrides that H(D) atoms occupy only *g* sites at medium hydrogen concentrations, as observed for ZrV_2D_x deuterides with $2.2<x<2.7$ in the temperature range 260-350 K [31].

The positional parameters x and z of deuterium atoms in 96*g* sites are very close to the corresponding "ideal" values, x = 0.063 and z = 0.875, derived for the case of the close packing of the metal atoms considered as hard spheres [32]. The displacements of D atoms from the "ideal" positions are assumed to be dependent on the deviation of R_A/R_B ratio from

its "ideal" value (1.225 for Laves phase compounds). For the studied (Zr,Ti,V)(Ni,Mn,Fe,V)$_2$-D deuteride, the value of R_A/R_B is 1.245, which is very close to the "ideal" value. For comparison, for C15-type $ZrCr_2D_{3.8}$ [33] with R_A/R_B = 1.250, x = 0.064, and z = 0.870, both the R_A/R_B ratio and the positional parameters (x and z) are close to the corresponding "ideal" values and well agree with the results of the present study.

Our structural data for (Ti,Zr,V)(Ni,Mn,Fe,V)$_2D_{2.9}$ at 300 K show that the closest distances between the filled by D atoms 96*g* interstices are r_{g1}= 1.174 (2) Å and r_{g2}= 1.314 (3) Å. The sublattice of *g* sites in the cubic Laves type phases consists of hexagons [34], in which r_{g1} characterizes the nearest sites within one hexagon and r_{g2} characterizes the next nearest sites. These sites are never simultaneously filled by H/D, and the shortest "real" D-D distance is ~2.1 Å from the refined crystal structure data.

The distances between the D atoms and the surrounding metal atoms are 1.997 (3) and 2.013 (3) Å for 8*a* and 1.739 (2) Å for 16*d* sites, Zr/Ti/V-D and Ni/V/Mn/Fe-D, respectively. Being typical values for the Zr-based intermetallic hydrides intermetallic deuterides, they are close to the corresponding distances observed for $ZrFe_{1.96}Al_{0.04}D_{2.9}$: $r_{Zr\text{-}D}$ = 2.09 and $r_{Fe(Al)\text{-}D}$ = 1.75 Å [35].

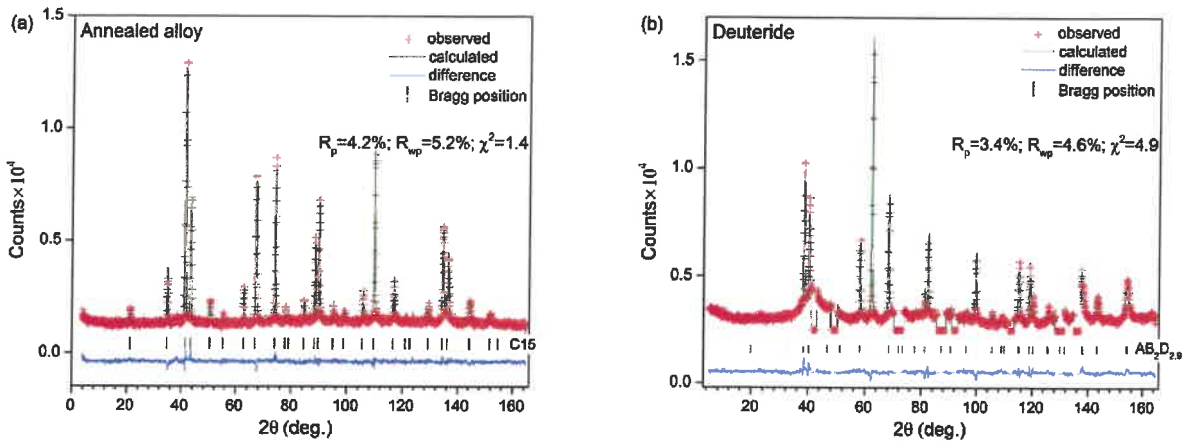

Fig. 2. Rietveld profile refinements of the neutron diffraction patterns of the initial AB_2 alloy (a) and its deuteride $AB_2D_{2.9}$ (b). The difference between the calculated and experimental profiles (line labeled "difference") are shown together with experimental points (+) and calculated profiles (green lines). The positions of the Bragg peaks are shown by ticks. (The peaks belonging to the sample holder were excluded from the refinements shown in Figure 2b).

Table 2

Crystallographic data for AB_2 phase and $AB_2D_{2.9}$ from the Rietveld profile refinements of the neutron diffraction presented in Fig. 2.

Atoms	Crystal structure parameters	$(Ti,Zr,V)(Ni,Mn,Fe,V)_2$	$(Ti,Zr,V)(Ni,Mn,Fe,V)_2D_{2.9}$
	a (Å)	7.0163(1)	7.5072(1)
	Δa/a, %	-	7.00
	V (Å^3)	345.41(1)	423.08(2)
	ΔV/V, %	-	22.5
Ti/Zr/V	Occupancy	0.213(2)/0.751(2)/0.036(2)	0.213/0.751/0.036
8*a* (1/8, 1/8, 1/8)	U_{iso}×100 (Å^2)	1.09(3)	0.77(6)
Ni/Mn /Fe/V	Occupancy	0.564(5)/0.338(5)/0.058(5)/0.040(5)	0.564/0.338/0.058/0.040
16*d* (1/2, 1/2, 1/2)	U_{iso}×100 (Å^2)	0.28 (2)	1.64(5)
D	Occupancy	-	0.239(1)
96*g* (x, x, z)	U_{iso}×100 (Å^2)	-	3.76(9)
	x, z	-	0.0631(4), 0.8716(6)
D content	-	-	2.87(1) at.D/f.u.

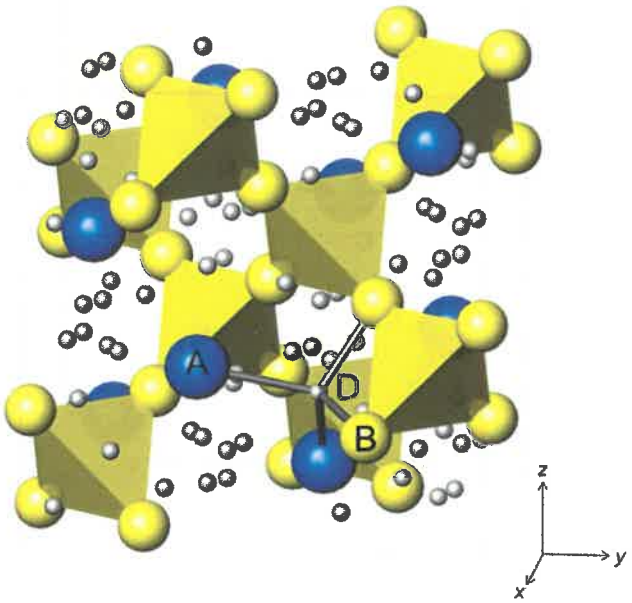

Fig. 3. The crystal structure of the cubic $AB_2D_{2.9}$ deuteride. D atoms partially, 24%, fill 96*g* sites shown as small spheres. A, B and D represent Zr/Ti/V (8a), Ni/Mn/Fe/V (16d), and D atoms, respectively. Spatial framework of B_4 tetrahedra is shown.

3.3. Microstructural characterization

The microstructure for the annealed alloy was studied by SEM using the backscattered electrons imaging, and the results are shown in Fig. 4a. According to the EDS analysis of the annealed alloy (see the data of Table 3), the darker region represents the major AB_2 phase. From the element composition in a lighter region, we conclude that this region is enriched by La, Ni and Mn coexisting in the formed La(Ni,Mn) phase. Furthermore, a formation of a small amount of ZrNiMn can also be the case as element analysis shows also presence of some Zr in the region 1. This is similar to the earlier reported data [3, 36]. Formation of a secondary La(Ni,Mn) phase is caused by the fact that La is nearly insoluble in Laves phase Zr/Ti-based intermetallics [37, 38].

Table 3

EDS compositional analysis data for the annealed alloy (at.%)

Region	Ti	Zr	La	Ni	Mn	V	Fe
1	0	18.4	31.9	37.0	12.7	0	0
2	6.7	23.6	0	40.1	20.8	3.8	5.0

Figures 4c–i show the EDX elemental mapping of Zr, Ti, La, Ni, Mn, V, and Fe. Distribution of La converges to the bright region, whereas Zr atoms are mainly located in the dark area. The distribution of Ni and Mn is slightly different between the bright and dark regions, but they both are present in the region 1 belonging to the secondary phase. This outcome is consistent with SEM results.

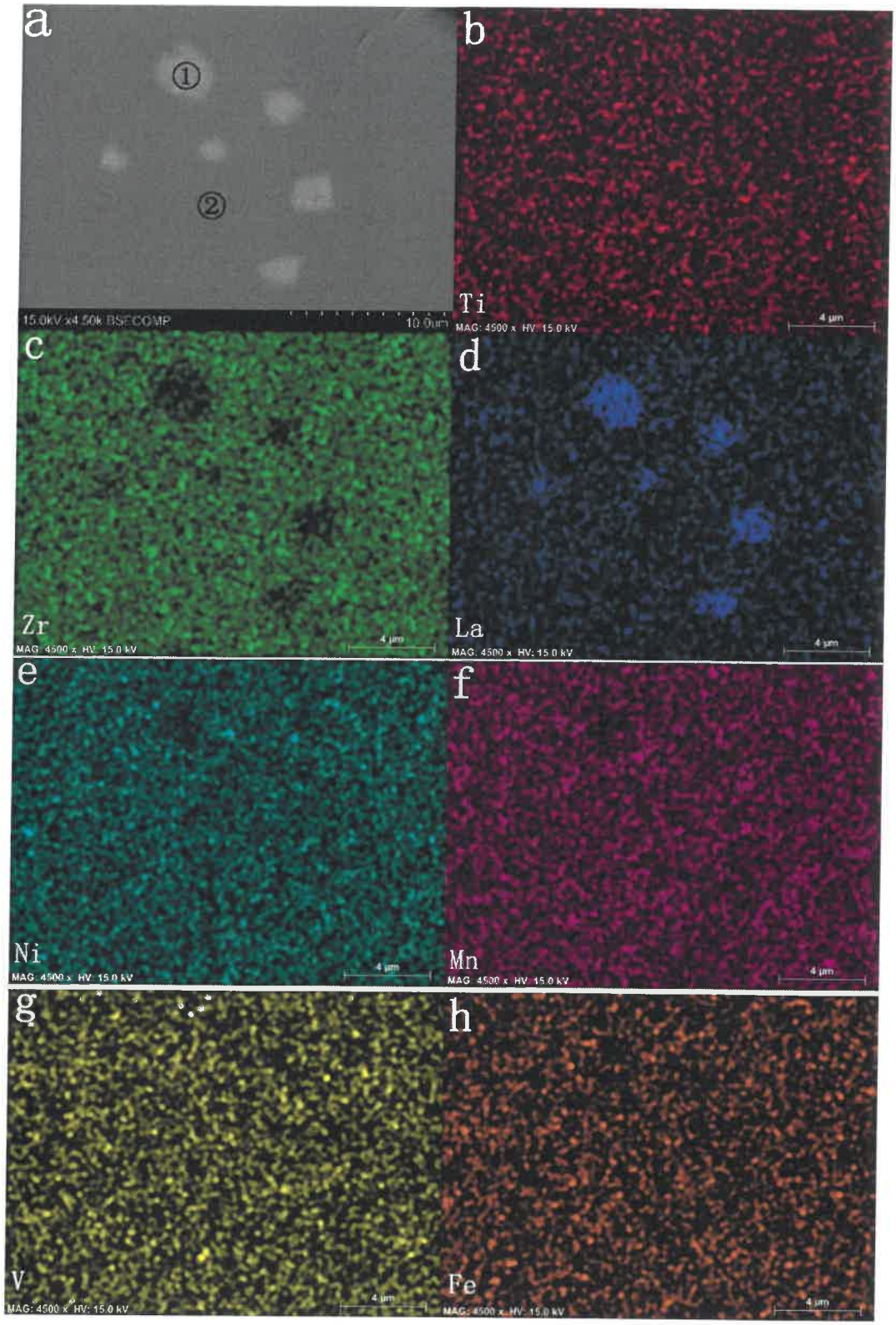

Fig. 4. SEM/BSE images (a) of the annealed alloy, and EDX mappings of Ti (b), Zr (c), La (d), Ni (e), Mn (f), V (g) and Fe (h), respectively.

4. Electrochemical characterization

4.1. Electrochemical performance

For studies and optimization of the effect of La addition on the electrochemical performance of the anodes, we prepared a series of Zr/Ti-based AB_2 alloys. These included $Ti_{0.2}Zr_{0.8}La_xNi_{1.2}Mn_{0.7}V_{0.12}Fe_{0.12}$ (x=0, 0.01, 0.03 and 0.05) alloys which for convenience are labeled as La0, La1, La3 and La5 (see Fig. 5a and b). The ratio between the components Ti/Zr/Ni/Mn/V/Fe is these alloys was kept unchanged, while the content of La was variable reaching 0.05 in maximum.

Figure 5a shows that the changes in La content significantly affect their activation behaviors of the studied alloys. For La-free AB_2 (La0) alloy the activation was slow and has not been completed during the first 10 cycles. The capacity gradually increased with further cycling reaching a maximum of 290 mAh/g at 0.71 C (1 C= 420 mAh/g; see Fig. 5b) after the number of cycles increased to 60.

In contrast, adding lanthanum to the composition of the alloy has a dramatic effect causing a significant improvement of the activation performance even at the smallest La content in the La1 alloy. Indeed, for La1 it took 8 activation cycles to reach the maximum capacity. With further increase in La content a full activation of the La3 alloys was reached already at 6 cycles, and for the La5 alloy only 4 cycles were required to accomplish the activation. Thus, we conclude that increase of La content to La5 step-by-step improves the activation behavior.

On the other hand, it appears that maximum discharge capacity first increases from La0 to La1 (290 → 380 mAh/g) and then after reaching a similar value for La3 (360 mAh/g) it significantly decreases to 310 mAh/g for La5. Thus, even though the highest content of La addition in La5 alloy accelerates the activation, it also leads to the obvious decrease of discharge capacity. Thus, we conclude that a proper addition of La to the alloy is in a range between 1 and 3 %, as in the La1 and La3 alloys, since this improves the activation performance, while allowing to reach a high discharge capacity.

The characterization of the alloys with variable La content showed that when doped with the lowest amount of lanthanum metal, La oxide phase is formed because of a high affinity of La to oxygen*) [39], as oxygen is present in the alloy as a metallurgical contamination. This purifies the alloys surface and intergranular area and makes the alloy's activation easier. Hence, we can assume that the formation of La oxide (or La oxyhydroxide in the hydrogenated alloy) and presence of LaNi intermetallic play an important role in catalyzing of the charging of the alloy by hydrogen causing improvement of the electrochemical performance of the anode material. However, when La content is further increased in the La5 alloy, the amount of the formed intermetallic LaNi secondary phase is growing further and this strongly affects various features of its electrochemical performance. Detailed data presenting the studies of the effect of the amount of added lanthanum on the electrochemical properties of the La-doped alloys will be presented in a separate publication [40].

---

*) For La_2O_3 heat of formation per 1 mol O (597.75 kJ/mol O) is 8.6 % higher than for ZrO_2 (550.4 kJ/mol O). Thus, thermodynamically formation of La_2O_3 is preferable to ZrO_2.

Figure 5b shows the cycling stability of the activated alloys at a charge-discharge density of 0.71 C (300 mA/g). Because of the increased discharge current density, the initial discharge capacities of all activated alloys slightly decreased as compared to the data collected at 0.24 C (see Figure 5a). With increasing of the number of the performed cycles, all alloys show a close to linear time-dependent degradation. As mentioned earlier, the electrochemical performance of the alloys is very much dependent on the La content. Indeed, La-free AB_2 alloy needs around 60 cycles to reach its maximum discharge capacity. With increasing amount of La starting already from La1 alloy, the activation becomes significantly improved. Furthermore, the content of La affects the cycling stability. The La5 alloy with the highest amount of the secondary LaNi phase present shows the lowest cycling stability, with only 43.7% of the initial capacity remaining after 500 charge/discharge (C/D) cycles. In contrast, after 500 charge-discharge cycles, both La1 and La3 alloys show a much higher capacity retention, with the reversible discharge capacity of La3 alloy showing a slightly better stability (63 % of the initial capacity) as compared to the La1 alloy anode (60 %). Thus, as the La3 alloy shows a better cycling stability during the 500 C/D cycles and a good activation behavior, as compared with other studied alloys, and the highest electrochemical discharge capacity of 420 mAh/g, in the following sections, we will focus on the characterization of the La3 alloy ($Ti_{0.2}Zr_{0.8}La_{0.03}Ni_{1.2}Mn_{0.7}V_{0.12}Fe_{0.12}$) only.

Figures 6a and 6b show the high-rate dischargeability (HRD) of the activated La3 alloy. 10 activation cycles at 0.24 C were completed for the alloy before studying its HRD characteristics. Fig. 6a shows the relationship between the applied potential and the discharge capacity, whereas Fig. 6b shows the dependence between the discharge capacity and the current density. At a low-rate current density of 10 mA/g, the full discharge capacity

corresponds to the hydrogen storage capacity of 1.51 wt.% H reached for the AB_2 Laves phase hydride having a composition $AB_2H_{2.9}$. This corresponds to the approximate value of 420 mAh/g for the electrochemical discharge capacity; this discharge capacity drops following an increase of the discharge current densities. The discharge capacities range from 370 mAh/g to 270 mAh/g at a discharge current density of 0.12 – 0.95 C (50 – 400 mA/g). It should be furthermore mentioned that the alloy displays a broad and flat discharge plateau allowing to maintain a nearly constant voltage during the discharge making the anode material very attractive for practical applications.

At the high-rate current densities (i.e., 100, 200, and 300 mA/g), the discharge capacities remain high, showing the level of 86%, 83%, and 79% of the maximum capacity (360, 350, and 330 mAh/g, respectively). In contrast, in the La-free AB_2 alloys [41, 42], the discharge capacities are quite low, around 148 and 228 mAh/g at a discharge current density of 300 mA/g. Thus, these results indicate that La additions can significantly improve the HRD performance of AB_2 alloys.

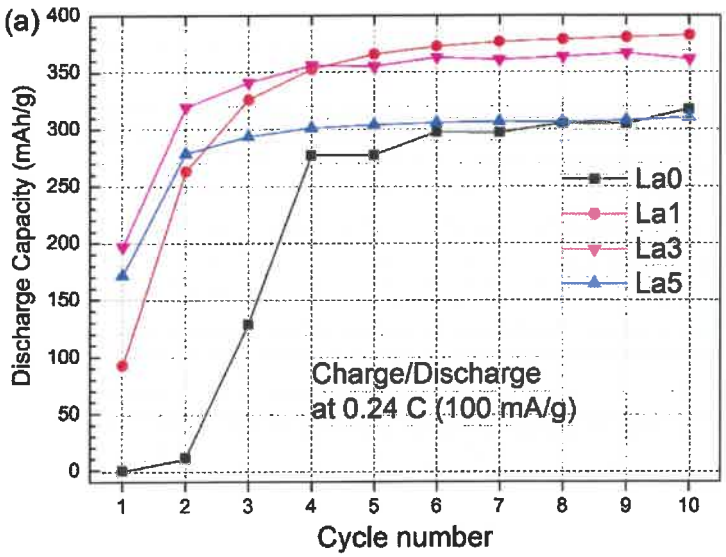

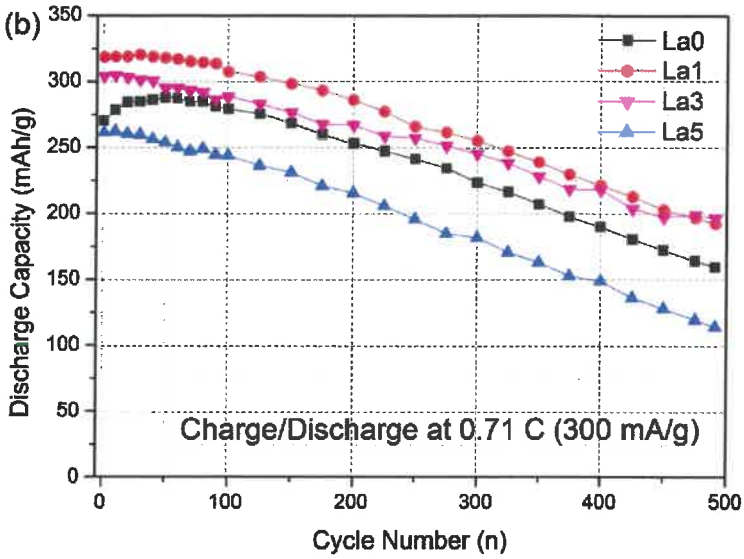

Fig. 5. The activation performance (a), and cycling stability (b) of the annealed alloy after performing 10 activation cycles.

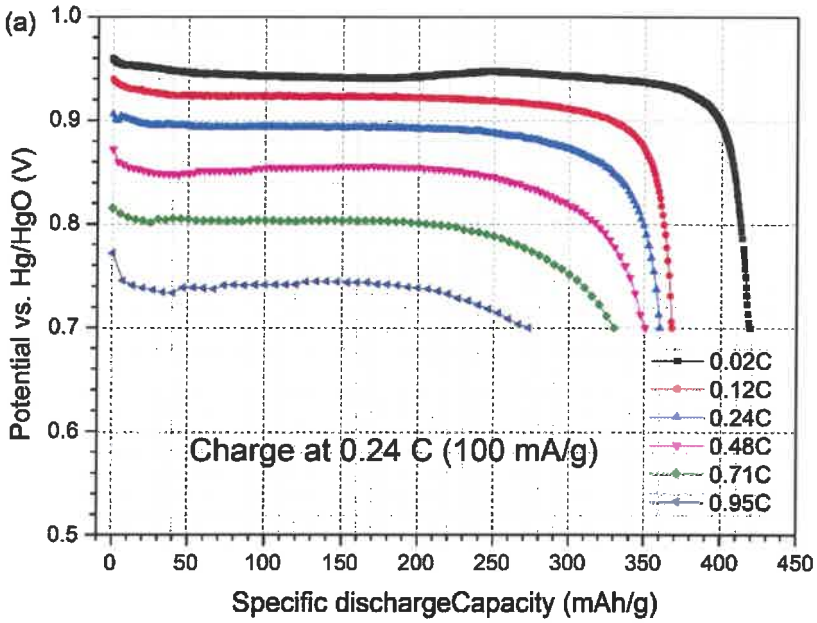

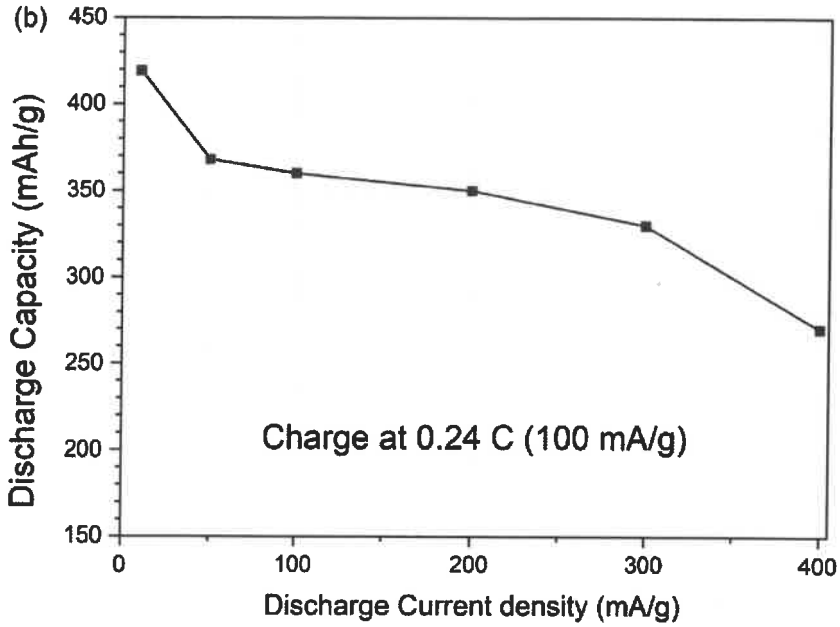

Fig. 6. High-rate discharge (HRD) performance of the annealed La3 alloy, shown as a relationship between the applied potential and discharge capacity (a), and as a relationship between the discharge capacity and the current density (b).

4.2. Electrochemical kinetics and Electrochemical Impedance Spectroscopy (EIS) studies of the cycled electrodes

HRD ability of the Ni/MH batteries is closely related to the kinetics of corresponding hydrogen absorption/desorption reactions [43, 44]. Potentiostatic discharge and linear polarization experiments were performed to further study the electrochemical kinetic properties of the hydrogenated alloys after performing 10, 100, 350, and 500 cycles.

The exchange current (I_0) of the reaction at hydride electrode can be determined using the linear polarization curves, according to the following expression (1) [3, 45].

$$I_0 = \frac{IRT}{F\eta} \qquad (1)$$

where R is the universal gas constant, T is the absolute temperature, I is the applied current density, F is the Faraday constant and η is the overpotential of the electrochemical reaction. When the overpotential is changed within a small range of ±10 mV, the current shows a linear dependence from the overpotential as is presented in Fig. 7a. This allows to accurately determine the values of exchange current (I_0). In the linear polarization experiments, the electrodes were fully charged, discharged to 50 % DOD, and then scanned within a narrow overpotential range, ±10 mV.

The hydrogen diffusion coefficient, which has an important effect on the C/D reaction, was evaluated by the potentiostatic method when performing stepwise experiments. As shown in Fig. 7b, each curve can be divided into two time regions separated by the dashed vertical line. In the first region, the current quickly decreases due to the consumption of hydrogen at the surface of the electrode. However, in the second region the descending trend becomes rather sluggish and the anodic current (log i) reveals an approximately linear time (t) dependence. Then the hydrogen diffusion coefficient (D) can be derived according to the following equation (2) [3, 46]:

$$\log i = \log\left(\frac{6FD}{da^2}(C_0 - C_s)\right) - \frac{\pi^2}{2.303}\frac{D}{a^2}t \qquad (2)$$

where i, D, C_0, C_s, a, d and t are the diffusion current density (A/g), the hydrogen diffusion coefficient (cm^2/s), the initial hydrogen concentration in the bulk of the alloy (mol/cm^3), the

hydrogen concentration on the surface of the alloy particles (mol/cm^3), the alloy particle radius (cm), the density of the alloy (g/cm^3), and the discharge time (s), respectively.

To satisfy the conditions for a pure diffusion control process, the fully charged electrode was discharged at a constant anodic potential of E=-0.6 V vs. Hg/HgO for a time of up to 3600 s. After adopting the average particle radius as a=50 μm, the hydrogen diffusion coefficient D was calculated using the above equation (2).

As shown in Table 4, during continuous cycling, D and I_0 increase after the first 100 cycles and then decrease. D and I_0 are related to the rates of hydrogen exchange in the alloy. However, D and I_0 are also affected by the change in the reaction area resulting from the disintegration of alloy particles. Progressing pulverization of alloy particles can provide more reaction area, and then lead to the increase of D and I_0. However, severe pulverization can increase the length of diffusion paths for H atoms, hence resulting in the decreases of D and I_0. Moreover, the capacity loss of the cycled alloy, which is experimentally observed on cycling, will decrease the values of D and I_0.

The exchange current density (I_0) for the metal hydride anode electrode is used to characterize the electrocatalytic activity for the charge transfer reaction at the metal/electrolyte interface. In general, the MH alloy particles during charge and discharge undergo a significant expansion and contraction. For the alloy studied in this work this value during a formation of the hydride from the alloy is as large as 22.5 vol. %. This expansion initiates the (micro)cracks which cause pulverization of the alloy. Such behavior is standard and has been reported for the other metal hydrides, for example, in [47, 48].

The increase in the reaction surface area resulting from pulverization should lead to the increase of the hydrogen exchange current density (I_0). This is indeed taking place as I_0 increases from 49.3 to 55.8 mA/g when the number of applied cycles is increasing from 10 to 100, respectively (see Table 4). However, when the number of cycles increases further from 100 to 500 cycles, I_0 shows a continuous decrease (Table 4). This suggests that the electrocatalytic activity of the alloy shows a significant dependence from the cycling history of the anode electrodes. It initially increases and reaches maximum after 100 cycles and then decreases on further cycling when the number of cycles is between100 and 500 cycles. The surface processes were further studied using EIS. Fig. 8 shows the electrochemical impedance spectra for the cycled alloys. Two resolved semi-circles emerge with progressing cycling. This is an indication of a presence of two distinct phases that participate in the electrochemical processes. Therefore, the equivalent circuit for the electrodes should consist of at least four components: electrolyte resistance (R_1), two resistive components (R_2 and R_{ct}), and a Warburg term (W_4) (insert in Fig. 8).

R_1 is the electrolyte resistance between the working and reference electrodes [49]. In the cycled alloys, R_1 generally increases with increased cycling, and this finding can be attributed to the change in electrolyte concentration during the cycling.

R_2 describes the contact resistance between a current collector and an alloy pellet, whereas R_3 is related to a particle-to-particle resistance in the pellet [49]. Therefore, we can estimate the mechanical deterioration, such as the disconnection of a pellet and a current collector

and disintegration of a pellet, by evaluating R_2 and R_3, respectively. With increased cycling, small changes in R_2 (just ~10% when increasing from 10 to 500 cycles) indicate that addition of carbonyl Ni powder to the anode electrodes effectively preserves the electrical contact between the alloy particles and current collectors. However, continuous and obvious increases (~370%) in R_3 show that a poor electrical contact between the alloy particles results from pulverization of the alloy electrodes during the cycling.

A change in the charge transfer reaction (oxidation/reduction process) resistance R_{ct} is caused by both a change in the reactivity of the alloy surface and a change in the reaction area resulting from disintegration of alloy particles [49]. With progressing cycling, although the loss of a relative number of the rechargeable alloy particles will increase R_{ct}, the increase in the reaction area will quite likely reduce R_{ct}.

In this study, after 100 C/D cycles, the pulverization of the alloy particles reduced the reaction resistance. With the increase in a number of cycles up to 350, the R_{ct} continuously reduced, because of a development of the pulverization. After 500 cycles, a very significant capacity loss was observed and is associated with the increase of R_{ct}. Further to a poor contact between the alloy particles resulting from the pulverization of the alloys, a mechanism of the deterioration of the Zr/Ti-based AB_2 alloy is considered to be caused by a reduced reactivity at the alloy's surface because of the progressing surface oxidation when in contact with alkaline solution.

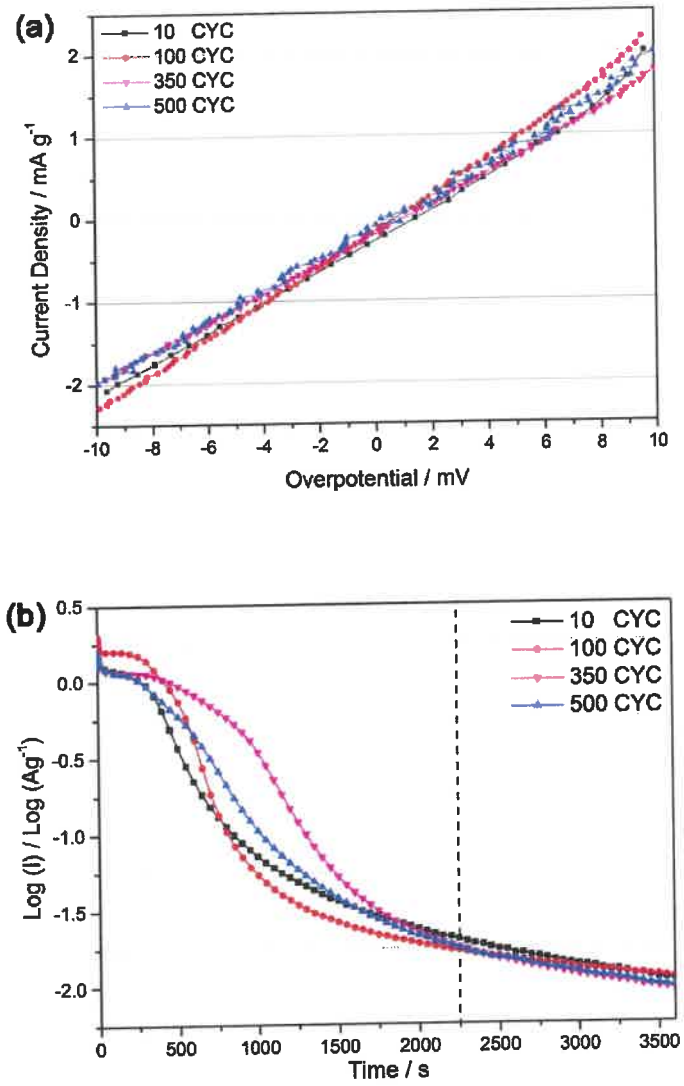

Fig. 7. Linear polarization curves (a) measured at 50% DOD and room temperature and semi-logarithmic plots (b) of anodic current vs. time for the La3 electrodes after different number of cycles.

Table 4

Summary data of the EIS studies for the cycled La3 electrode: the exchange current density I_0, the hydrogen diffusion coefficient D and the resistances R_1, R_2, R_3, and R_{ct}, as refined using the equivalent circuit shown in Fig.8.

Number of cycles (N)	D ($\times 10^{-10}$ cm^2/s)	I_0(mA/g)	R_1 (Ω) (Ohm)	R_2 (Ω) (Ohm)	R_3 (Ω) (Ohm)	R_{ct} (Ω) (Ohm)
10	12.2	49.3	0.057	4.441	0.208	2.334
100	27.3	55.8	0.072	3.919	0.229	1.534
350	13.0	48.7	0.224	3.977	0.738	1.189
500	11.7	46.3	0.226	3.590	0.984	3.393

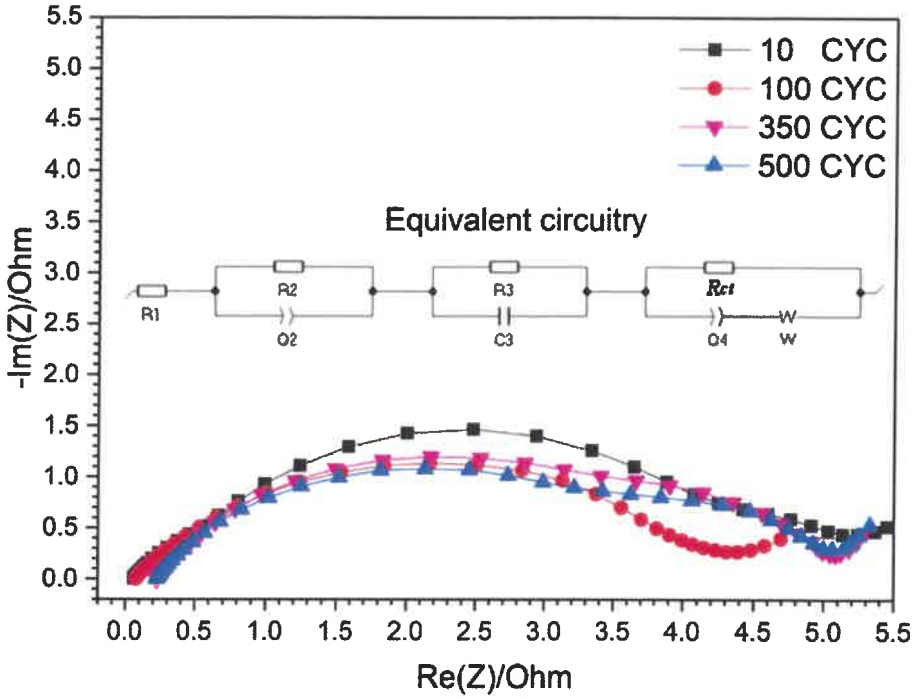

Fig. 8. The electrochemical impedance spectra measured at 298 K for the cycled La3 electrodes. The equivalent circuit for the half-cell measurement configuration used in this paper is shown as an inset.

CONCLUSIONS

In the present work, the La-doped AB_2 type alloys, $Ti_{0.2}Zr_{0.8}La_xNi_{1.2}Mn_{0.7}V_{0.12}Fe_{0.12}$ (x=0.01-0.05), were studied as metal hydride battery anode materials using XRD, NPD, SEM/EDX, and electrochemical characterization.

XRD study showed that the studied alloys consist of a C15 Laves type intermetallic. Metallurgical characterization demonstrated the presence of LaNi secondary intermetallic in the annealed AB_2 alloys, and this phase played an important role in improved charge-discharge performance of the La3 alloy, particularly in its easier activation.

Neutron diffraction study of the intermetallic La3 alloy and its deuteride $(Ti,Zr,V)(Ni,Mn,Fe,V)_2D_{2.9}$ also crystallizing with C15-type structure showed that D atoms occupy one type of tetrahedral interstitial sites, 96*g*, with A_2B_2 surrounding and V atoms occupying both 8*a* and 16*d* sites.

Adding La to the composition of the alloy causes a dramatic improvement of the activation performance even at the smallest La content (x=0.01). For La5 alloy activation period was shortened to just 4 cycles, but an excessive amount of La led to the obvious decrease of discharge capacity and cycling stability, even though no significant oxidation took place for the cycled electrodes.

Although the La1 and La3 alloys showed the similar improved activation and discharge capacities, the La3 alloy displayed a better capacity retention, 63 % of the initial capacity,

after 500 C/D cycles. At a low-rate current density of 10 mA/g, the La3 alloy shows a full discharge capacity of 420 mAh/g corresponding to the hydrogen storage capacity of 1.51 wt.% H. At the high-rate current densities, 200 and 300 mA/g, the discharge capacities of the La3 alloy remain at a high level of 83% and 79% of the maximum capacity (350, and 330 mAh/g, respectively).

The D and I_0 of the cycled electrode show an increase after 100 cycles followed by their decrease on further cycling, after 350 and 500 cycles. Step-by-step drops in the electrochemical characteristics of the AB_2 alloy are related to a reduced reactivity of the alloy's surface and pulverization of the alloy particles on cycling.

The findings of this work will contribute to the optimization of the advanced AB_2-type Laves phase alloys as battery anodes for the metal hydride batteries.

ACKNOWLEDGEMENTS

This work is partly based on the NPD experiments performed at the Swiss spallation neutron source SINQ, Paul Scherrer Institute, Villigen, Switzerland. We are grateful to Dr. Denis Sheptyakov (PSI) for his help during the experiments.

This work was supported by the Norwegian Research Council (project "High Power Batteries Probed by Neutron Scattering", program SYNKNØYT; RCN project 234246), IEA Task 32 project Hydrogen Based Energy Storage (RCN project 285146) and Norwegian Research Center on Zero Emission Energy Systems for Transport – FME MoZEES.

This work was also financially supported by the National Natural Science Foundation of China (Grant No. 11605007). C.B. Wan acknowledges the funding received from the project No. 201506465019 by China Scholarship Council (CSC).

REFERENCES

[1] V. Yartys, D. Noreus, M. Latroche, Appl. Phys. A, 122 (2016) 1-11.

[2] Y. Liu, H. Pan, M. Gao, Q. Wang, J. Mater. Chem., 21 (2011) 4743-4755.

[3] K. Young, D.F. Wong, T. Ouchi, B. Huang, B. Reichman, Electrochim. Acta, 174 (2015) 815-825.

[4] B. Zhang, Y. Wu, Progress in Natural Science: Materials International, 27 (2017) 21-33.

[5] H. Zhang, X. Zheng, X. Tian, Y. Liu, X. Li, Progress in Natural Science: Materials International, 27 (2017) 50-57.

[6] K. Hong, J. Power Sources, 96 (2001) 85-89.

[7] Y.L. Du, X.G. Yang, Q.A. Zhang, Y.Q. Lei, M.S. Zhang, Int. J. Hydrogen Energy, 26 (2001) 333-337.

[8] M. Yoshida, E. Akiba, J. Alloys Compd., 224 (1995) 121-126.

[9] J.C. Sun, S. Li, S.J. Ji, J. Alloys Compd., 446–447 (2007) 630-634.

[10] D.F. Wong, K. Young, J. Nei, L. Wang, K.Y.S. Ng, J. Alloys Compd., 647 (2015) 507-518.

[11] W.-X. Chen, J. Alloys Compd., 319 (2001) 119-123.

[12] A.A. Volodin, C. Wan, R.V. Denys, G.A. Tsirlina, B.P. Tarasov, M. Fichtner, U. Ulmer, Y. Yu, C.C. Nwakwuo, V.A. Yartys, Int. J. Hydrogen Energy, 41 (2016) 9954-9967.

[13] A.C. Larson, R.B.V. Dreele, Los Alamos National Laboratory Report LAUR (2004) 86-748.

[14] P. Fischer, G. Frey, M. Koch, M. Könnecke, V. Pomjakushin, J. Schefer, R. Thut, N. Schlumpf, R. Bürge, U. Greuter, S. Bondt, E. Berruyer, Physica B: Condensed Matter, 276–278 (2000) 146-147.

[15] C. Wan, V.E. Antonov, R.V. Denys, V.I. Kulakov, V.A. Yartys, Progress in Natural Science:

Materials International, 27 (2017) 74-80.

[16] W.K. Hu, R.V. Denys, C.C. Nwakwuo, T. Holm, J.P. Maehlen, J.K. Solberg, V.A. Yartys, Electrochim. Acta, 96 (2013) 27-33.

[17] J.M. Joubert, M. Latroche, A. Percheron-Guégan, J. Bouet, J. Alloys Compd., 240 (1996) 219-228.

[18] K. Young, T. Ouchi, X. Lin, B. Reichman, J. Alloys Compd., 655 (2016) 50-59.

[19] K. Young, T. Ouchi, B. Huang, B. Reichman, M.A. Fetcenko, Int. J. Hydrogen Energy, 36 (2011) 12296-12304.

[20] K. Young, D.F. Wong, S. Yasuoka, J. Ishida, J. Nei, J. Koch, J. Power Sources, 251 (2014) 170-177.

[21] K. Young, T. Ouchi, B. Huang, B. Reichman, M.A. Fetcenko, J. Power Sources, 196 (2011) 8815-8821.

[22] K. Young, J. Koch, S. Yasuoka, H. Shen, L.A. Bendersky, J. Power Sources, 277 (2015) 433-442.

[23] L. Kong, B. Chen, K. Young, J. Koch, A. Chan, W. Li, J. Power Sources, 213 (2012) 128-139.

[24] Y. Nakamura, K. Oguro, I. Uehara, E. Akiba, J. Alloys Compd., 298 (2000) 138-145.

[25] S.L. Li, W. Chen, G. Luo, X.B. Han, D.M. Chen, K. Yang, W.P. Chen, Int. J. Hydrogen Energy, 37 (2012) 3268-3275.

[26] Z.L. Chen, T.Z. Si, Q.A. Zhang, J. Alloys Compd., 621 (2015) 42-46.

[27] S. Suwarno, J.K. Solberg, B. Krogh, S. Raaen, V.A. Yartys, Int. J. Hydrogen Energy, 41 (2016) 1699-1710.

[28] H. Nakamura, Y. Nakamura, S. Fujitani, I. Yonezu, Int. J. Hydrogen Energy, 21 (1996) 457-460.

[29] S. Suwarno, J.K. Solberg, J.P. Mæhlen, R.V. Denys, B. Krogh, E. Ochoa-Fernández, B.T. Børresen, E. Rytter, I.E. Gabis, V.A. Yartys, Int. J. Hydrogen Energy, 38 (2013) 14704-14714.

[30] S. Suwarno, J.K. Solberg, J.P. Maehlen, B. Krogh, B.T. Børresen, E. Ochoa-Fernandez, E. Rytter, M. Williams, R. Denys, V.A. Yartys, Transactions of Nonferrous Metals Society of China, 22 (2012) 1831-1838.

[31] A.V. Irodova, G. Andre, F. Bouree, J. Alloys Compd., 350 (2003) 196-204.

[32] A.V. Skripov, J.C. Cook, T.J. Udovic, M.A. Gonzalez, R. Hempelmann, V.N. Kozhanov, J. Phys.: Condens. Matter, 15 (2003) 3555.

[33] V.A. Yartys, V.V. Burnasheva, K.N. Semenenko, N.V. Fadeeva, S.P. Solov'ev, Int. J. Hydrogen Energy, 7 (1982) 957-965.

[34] A.V. Skripov, J.C. Cook, D.S. Sibirtsev, C. Karmonik, R. Hempelmann, J. Phys.: Condens. Matter, 10 (1998) 1787.

[35] V.A. Yartys, R.V. Denys, C.J. Webb, J.P. Mæhlen, E.M. Gray, T. Blach, O. Isnard, L.C. Barnsley, J. Alloys Compd., 509 (2011) S817-S822.

[36] J. Nei, K. Young, S.O. Salley, K.Y.S. Ng, Mater. Chem. Phys., 136 (2012) 520-527.

[37] D. Sun, J.M. Joubert, M. Latroche, A. Percheron-Guégan, J. Alloys Compd., 239 (1996) 193-197.

[38] D. Sun, M. Latroche, A. Percheron-Guégan, J. Alloys Compd., 248 (1997) 215-219.

[39] George C. Fitzgibbon, Charles E. Holley, Jr., *J. Phys. Chem.*, 1965, 69 (7), pp 2464-2466; Elmer J. Huber Jr., Earl L. Head, and Charles E. Holley Jr. *J. Phys. Chem.*, 1964, 68 (10), pp

3040–3042

[40] C.B. Wan, R.V. Denys, V.A.Yartys, J. Alloys Compd., (2018). (In preparation).

[41] K. Shu, S. Zhang, Y. Lei, G. Lü, Q. Wang, J. Alloys Compd., 349 (2003) 237-241.

[42] J.C. Sun, S. Li, S.J. Ji, J. Alloys Compd., 404–406 (2005) 687-690.

[43] M. Tliha, H. Mathlouthi, C. Khaldi, J. Lamloumi, A. Percheron-guegan, J. Power Sources, 160 (2006) 1391-1394.

[44] F. Feng, D.O. Northwood, J. Power Sources, 136 (2004) 346-350.

[45] P.H.L. Notten, P. Hokkeling, J. Electrochem. Soc., 138 (1991) 1877-1885.

[46] G. Zheng, B.N. Popov, R.E. White, J. Electrochem. Soc., 142 (1995) 2695-2698.

[47] M. Tliha, H. Mathlouthi, J. Lamloumi, A. Percheron-Guegan, J. Alloys Compd., 436 (2007) 221-225.

[48] P.H.L. Notten, R.E.F. Einerhand, J.L.C. Daams, J. Alloys Compd., 231 (1995) 604-610.

[49] N. Kuriyama, T. Sakai, H. Miyamura, I. Uehara, H. Ishikawa, T. Iwasaki, J. Alloys Compd., 202 (1993) 183-197.

Figure captions in the paper

Electrochemical studies and phase-structural characterization of a high-capacity La-doped AB_2 Laves type alloy and its hydride

by

ChuBin Wan, R.V. Denys, M. Lelis, D. Milčius, V.A.Yartys

Figure 1.

Rietveld refinements of XRD profiles for the annealed alloy (a), after performing cycling of charge-discharge - 30 cycles (b) and 500 cycles (c) - of the alloy anode. Vertical ticks show the positions of the Bragg peaks of the phase constituents (C15 Laves type intermetallic and Ni foam).

Figure 2.

Rietveld profile refinements of the neutron diffraction patterns of the initial AB_2 alloy (a) and its deuteride $AB_2D_{2.9}$ (b). The difference between the calculated and experimental profiles (line labeled "difference") are shown together with experimental points (+) and calculated profiles (green lines). The positions of the Bragg peaks are shown by ticks. (The peaks belonging to the sample holder were excluded from the refinements shown in Figure 2b).

Figure 3.

The crystal structure of the cubic $AB_2D_{2.9}$ deuteride. D atoms partially, 24%, fill 96*g* sites shown as small spheres. A, B and D represent Zr/Ti/V (8a), Ni/Mn/Fe/V (16d), and D atoms, respectively. Spatial framework of B_4 tetrahedra is shown.

Figure 4.

SEM/BSE images (a) of the annealed alloy, and EDX mappings of Ti (b), Zr (c), La (d), Ni (e), Mn (f), V (g) and Fe (h), respectively.

Figure 5.

The activation performance (a), and cycling stability (b) of the annealed alloy after 10 activation cycles.

Figure 6.

High-rate discharge (HRD) performance of the annealed La3 alloy, shown as a relationship between the applied potential and discharge capacity (a), and as a relationship between the discharge capacity and the current density (b).

Figure 7.

Linear polarization curves (a) measured at 50% DOD and room temperature and Semi-logarithmic plots (b) of anodic current vs. time for the La3 electrodes after different number of cycles.

Figure 8.

The electrochemical impedance spectra measured at 298 K for the cycled La3 electrodes. The equivalent circuit for the half-cell measurement configuration used in this paper is shown as an inset.

Table 1

Table 1.

Crystallographic data obtained during Rietveld refinements of the annealed alloy, and the electrodes containing this alloy after performing 30 and 500 cycles.

Samples	Phase	Space group	Unit cell parameters	
			a, Å	V, Å^3
Annealed alloy	C15	$Fd\bar{3}m$	7.0441(1)	349.52(1)
After 30 cycles	C15	$Fd\bar{3}m$	7.0159(1)	345.34(1)
After 500 cycles	C15	$Fd\bar{3}m$	7.0096(0)	344.41(1)

Metal Ni phase present in a sample as a Ni foam is identified in the cycled electrodes but is not listed in Table 1 for simplicity. Abundance of the refined intermetallic was 100 % in each case.

Table 2

Table 2

Crystallographic data for AB_2 phase and $AB_2D_{2.9}$ from the Rietveld profile refinements of the neutron diffraction presented in Fig. 2.

Atoms	Crystal structure parameters	$(Ti,Zr,V)(Ni,Mn,Fe,V)_2$	$(Ti,Zr,V)(Ni,Mn,Fe,V)_2D_{2.9}$
	a (Å)	7.0163(1)	7.5072(1)
	Δa/a, %	-	7.00
	V (Å^3)	345.41(1)	423.08(2)
	ΔV/V, %	-	22.5
Ti/Zr/V	Occupancy	0.213(2)/0.751(2)/0.036(2)	0.213/0.751/0.036
8*a* (1/8, 1/8, 1/8)	U_{iso}×100 (Å^2)	1.09(3)	0.77(6)
Ni/Mn /Fe/V	Occupancy	0.564(5)/0.338(5)/0.058(5)/0.040(5)	0.564/0.338/0.058/0.040
16*d* (1/2, 1/2, 1/2)	U_{iso}×100 (Å^2)	0.28 (2)	1.64(5)
D	Occupancy	-	0.239(1)
96*g* (x, x, z)	U_{iso}×100 (Å^2)	-	3.76(9)
	x, z	-	0.0631(4), 0.8716(6)
D content	-	-	2.87(1) at.D/f.u.

Table 3

Table 3

EDS compositional analysis data for the annealed alloy (at.%)

Region	Ti	Zr	La	Ni	Mn	V	Fe
1	0	18.4	31.9	37.0	12.7	0	0
2	6.7	23.6	0	40.1	20.8	3.8	5.0

Table 4

Summary data of the EIS studies for the cycled La3 electrode: the exchange current density I_0, the hydrogen diffusion coefficient D and the resistances R_1, R_2, R_3, and R_{ct}, as refined using the equivalent circuit shown in Fig.8.

Number of cycles (N)	D ($\times 10^{-10}$ cm^2/s)	I_0 (mA/g)	R_1 (Ω) (Ohm)	R_2 (Ω) (Ohm)	R_3 (Ω) (Ohm)	R_{ct} (Ω) (Ohm)
10	12.2	49.3	0.057	4.441	0.208	2.334
100	27.3	55.8	0.072	3.919	0.229	1.534
350	13.0	48.7	0.224	3.977	0.738	1.189
500	11.7	46.3	0.226	3.590	0.984	3.393

Figure 1a
Click here to download high resolution image

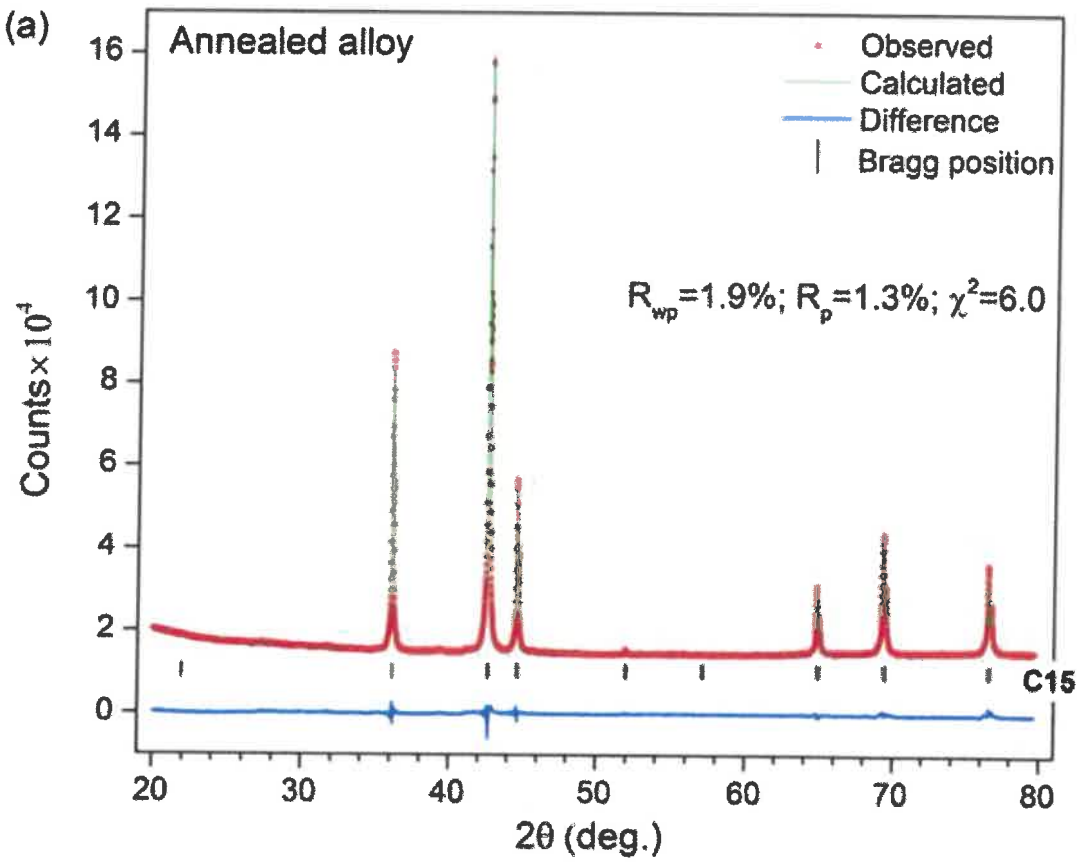

Graphical Abstract

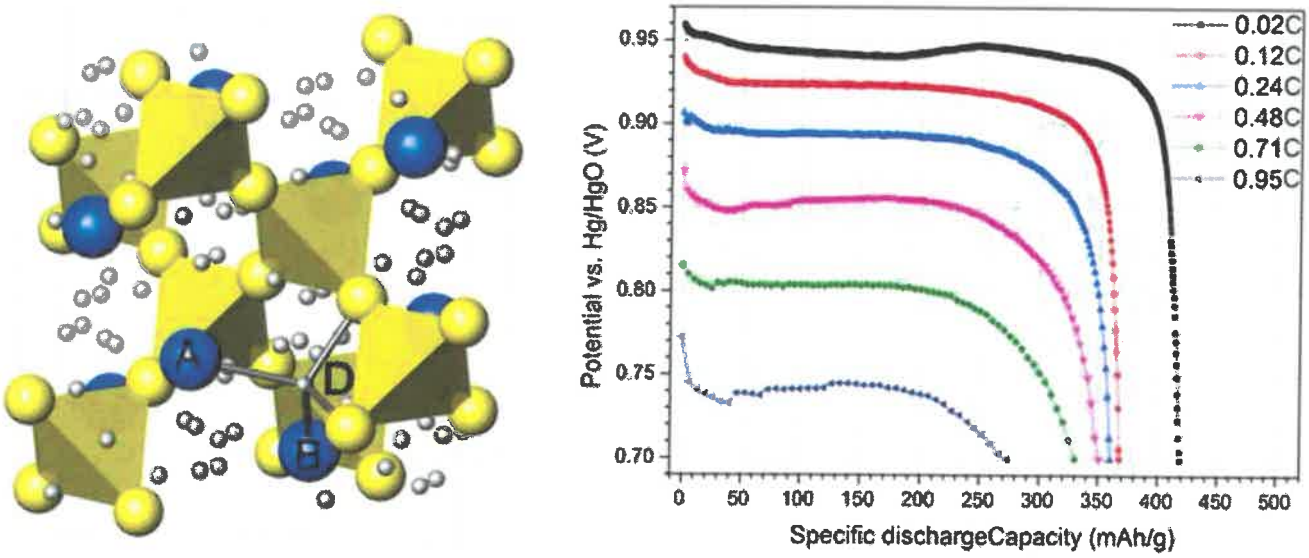

*Highlights (for review)

HIGHLIGHTS

- Annealed multi-component Zr/Ti-based alloy has a FCC C15 Laves type structure
- The maximum electrochemical discharge capacity of the alloy reaches 420 $mAhg^{-1}$
- La addition significantly improves the electrochemical performance of AB_2 alloy
- D atoms occupy the 96*g* sites only while V atoms occupy both 8*a* and 16*d* sites